Trends in Chemistry

CellPress

Review

2D Material Bubbles: Fabrication, Characterization, and Applications

Daniel A. Sanchez,[1] Zhaohe Dai,[2,3] and Nanshu Lu[1,2,4,*]

When 2D materials are supported by substrates, matter trapped at the interface can coalesce to form nano- and microscale bubbles. These bubbles often negatively impact the performance of 2D material devices as they impede charge/photon/phonon transport across the interface. The difficulties created by these bubbles spurred research to understand how they form, whether their formation can be controlled, and what kind of matter is trapped inside them. These 2D material bubbles have since been exploited for novel chemistry and physics because of their ability to pressurize the trapped matter and strain the confining 2D material. The fabrication, characterization, and applications of 2D material bubbles are summarized in this review.

Highlights

Gases, liquids, and solids trapped underneath 2D materials deform the atomically thin material into micro- and nano-bubbles. Bubbles can form spontaneously or in controlled manners. Direct and indirect methods were used to probe the chemical contents inside these bubbles.

There are a vast number of combinations possible for the 2D materials and trapped matter that form the bubble, which makes these bubbles a versatile platform for exploring rich nanoscale phenomena.

Bubbles are conducive for creating confined and pressurized environments to trap chemicals and induce chemical reactions at high temperature. Atomically thin 2D materials allow for the *in situ* transmission electron microscope (TEM) observation of these chemical reactions. Bubbles also alter the physical properties of the 2D materials due to the nonuniform strain fields they can generate.

Bubbles Made from 2D Materials

2D materials constitute the thinnest materials possible with thicknesses limited by the size of the atoms that make up their structures. Individual sheets of 2D materials are easily exfoliated from their naturally forming bulk crystals due to strong, in-plane covalent bonding within the sheet and relatively weak out-of-plane **van der Waals (vdW) bonding** (see Glossary) across sheets. Since the discovery of exfoliated graphene [1], the family of 2D materials has expanded to include 2D crystals synthesized by chemical vapor deposition (CVD) [2], amorphous 2D materials [3], 2D polymers [4], and more. These atomically thin sheets, each with unique electronic, mechanical, and optical properties, present a myriad of possibilities as they are stacked and rotated to form layered materials, the properties of which could be drastically different from the properties of the individual layers [5,6]. The performance of these materials greatly depends on the quality of their interfaces. For most 2D material devices, the interface should be atomically clean, such that no foreign matter obstructs contact between adjoining materials [7]. However, ensuring the cleanliness of 2D materials at the atomic scale remains a grand challenge. Nanoscale pockets of trapped matter, herein referred to as bubbles, often form after a 2D material is laminated onto a substrate [8,9]. The discovery of 2D material bubbles has inspired numerous studies to understand how they form, the phase and chemical composition of the trapped matter, and their possible use in chemistry, physics, and even devices.

Methods for Fabricating 2D Material Bubbles

Spontaneously Formed Bubbles

The most ubiquitous bubble fabrication method in the literature is the layering of 2D materials to trap molecules naturally adsorbed on their surfaces (Figure 1A) [10–14]; bubbles generated this way are referred to as 'spontaneously formed bubbles'. In general, this fabrication method starts with a 2D material supported by a stamp (i.e., a donor substrate), as well as a target substrate onto which the 2D material is transferred (Figure 1A,i). When exposed to ambient conditions, **adventitious contamination** adsorbs onto the surfaces of clean 2D material and substrates (Figure 1A,ii a) [15]. The stamp and target substrate are then brought into contact (Figure 1A,iii). After releasing the stamp, the 2D material is transferred onto the substrate given appropriate interfacial adhesions. The vdW attraction between the 2D material and substrate seals the interface and aggregates the interfacial contamination into bubbles (Figure 1A,iv) [13]. The sample

[1]Materials Science and Engineering Program and Texas Materials Institute, The University of Texas at Austin, Austin, TX 78712, USA
[2]Center for Mechanics of Solids, Structures, and Materials, Department of Aerospace Engineering and Engineering Mechanics, The University of Texas at Austin, Austin, TX 78712, USA
[3]Mathematical Institute, University of Oxford, Woodstock Rd, Oxford, OX2 6GG, UK
[4]Department of Biomedical Engineering, The University of Texas at Austin, Austin, TX 78712, USA

*Correspondence: nanshulu@utexas.edu (N. Lu).

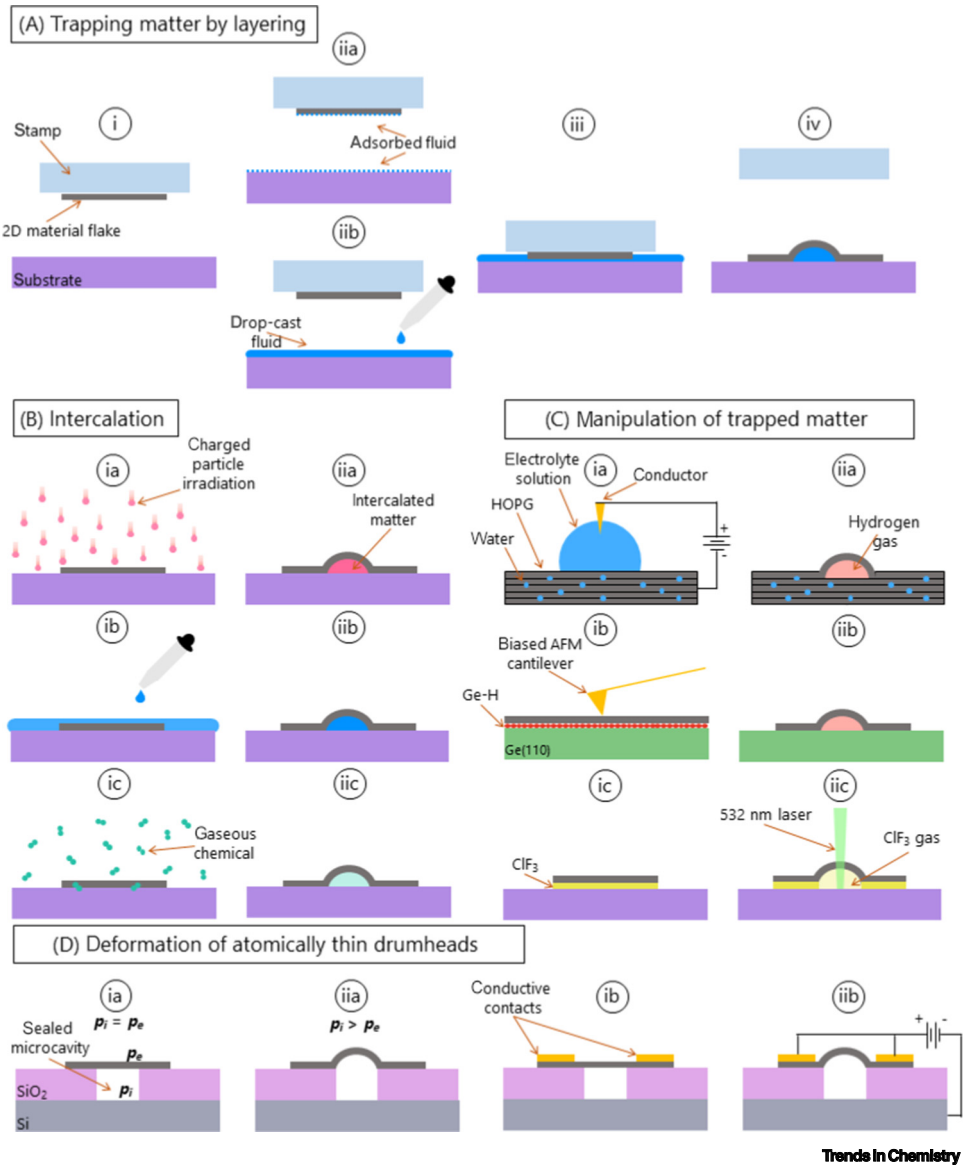

Figure 1. Summary of 2D Material Bubble Fabrication Methods. (A,i) A stamp carrying a 2D material. The 2D material traps substances that have either adsorbed (A,iia) or been intentionally introduced (A,iib) at adjoining surfaces. After the 2D material is stamped onto the substrate (A,iii), the van der Waals adhesion between the 2D material and the substrate forces the interfacial fluid to coalesce into bubbles (A,iv). (B) Matter is introduced into the 2D material–substrate interface by bombarding the surface with charged particle irradiation (B,a), immersing the sample in a desired fluid (B,b), or by introducing a gaseous chemical, such as water vapor, into the environment in which the sample is stored (B,c). (C) Matter already trapped at the interface is manipulated to form bubbles. Voltage-induced hydrolysis produces H_2 below the graphite surface to create gas-filled bubbles (C,a). A biased atomic force microscope (AFM) tip locally aggregates H_2 trapped in the graphene/Ge(110) interface, allowing for the precise control of where the bubbles form (C,b). ClF_3 trapped in the graphene/SiO_2 interface rapidly vaporizes when the area is excited with a laser, creating a gas-filled bubble (C,c). (D) Graphene is placed on an SiO_2 microwell to form a drumhead, which deforms into a bubble by either changing the pressure inside of the drumhead, p_i, relative to the environmental pressure, p_e, (D,a) or by applying an electric field (D,b). Abbreviation: HOPG, highly ordered pyrolytic graphite.

Glossary

Adventitious contamination: the adsorbed contamination that accumulates on surfaces when exposed to ambient conditions.

Direct-to-indirect band gap transition: the transition in the electronic structure of a material such that electrons hopping from the valence band to the conduction band require a change in momentum, typically from the electron–phonon interactions.

Elastocapillarity: the situation in which capillary forces from liquids are relatively large enough to cause elastic deformation in solid structures.

Laplace pressure: the pressure differential across a curved interface or surface.

Ostwald ripening: the spontaneous thermodynamic process in which smaller particles diffuse into larger particles.

Pseudomagnetic field (PMF): the nonuniform strain distributions in 2D materials that affect the transport properties of the electrons, analogous to the effect a magnetic field applied perpendicularly to the graphene basal plane would have on those electrons.

van der Waals (vdW) bonding: the attractive force between two bodies that varies with the separation of the two bodies in consideration. The forces that give rise to vdW bonding result from fluctuating dipole interactions between atoms that constitute the neighboring bodies.

may be processed further with thermal annealing to allow continued aggregation of the trapped contamination [8]. The cleanliness of the bubble-free regions of the interface remains contested; some studies suggest that the formation of bubbles indicates that the rest of the interface is clean and contamination-free [11,16], while others demonstrated that a thin layer of fluid could coexist with the bubbles in the interface [17,18]. The chemical nature of the bubble contents may also be designed by drop-casting a solution of the chemical of interest onto the substrate surface before stamping the 2D material (Figure 1A,iib) [19]. Nanoparticles can be added to the liquid to trap solid matter inside the bubbles as well [20]. Bubbles may also emerge in substrate-supported flakes as the flake degrades over time. In black phosphorus, the formation of bubbles has been attributed to the degradation-induced hydroxyl groups, which allow ambient contents such as water molecules to diffuse into the interface [21,22]. Transition metal dichalcogenides (TMDs) have been observed to form degradation-induced bubbles at different rates, depending on the material type, with MoS_2 having the longest ambient stability among the studied TMDs [23,24].

Induced Bubbles

In contrast to spontaneously formed bubbles, 2D material bubbles can also be intentionally induced in cases where the 2D material pre-exists on a desired substrate and a foreign liquid or gas is intercalated through the flake–substrate interface or across the membrane (Figure 1B). Exposing the substrate-supported flake to charged particle irradiation produces bubbles filled with the irradiated matter (Figure 1B,a). This method allows for a variety of trapped matter, including noble gases and H_2 [25–29]. Samples exposed to noble gas irradiation formed bubbles of varying sizes, with lateral dimensions ranging from a single atom [27] up to a few microns [25,28,30]. For bubbles fabricated using proton irradiation, Tedeschi and colleagues hypothesized that protons accelerated towards the 2D material penetrate through the basal plane. These intercalated protons form hydrogen molecules following the $2H^+ + 2e^- \rightarrow H_2$ reaction, where a ground contact to the sample supplies electrons for the reaction [25,31]. Alternatively, liquid or gas molecules could diffuse through the flake–substrate interface to form bubbles [17,32]. Kim and colleagues submersed graphene/SiO_2 samples into chloroform to create bubbles and speculated that the liquid penetrated through point defects, cracks, or through the sides of graphene to form inhomogeneous clusters (Figure 1B,b) [33]. Gaseous chemicals have also been hypothesized to travel through defects and edges of substrate-supported 2D materials (Figure 1B,c). Water-filled bubbles formed when graphene/SiO_2 samples were stored in high relative humidity environments [34]. Similarly, Lu and colleagues formed graphene bubbles on a Ru(0001) by introducing 90 Langmuir (L) of O_2 gas into the ultra-high vacuum chamber in which the sample was stored at an elevated temperature of 550 K [35].

Instead of introducing new materials to the interface, substances that are already trapped in the interface can be utilized to inflate the bubbles (Figure 1C). Water existing in the bulk of graphite has been hydrolyzed into gas-filled bubbles through voltage-induced water splitting (Figure 1C,a). The content of these bubbles can either be H_2 or O_2, depending on whether the graphite is set as the cathode or anode [36]. In another example, voltage applied through an atomic force microscope (AFM) tip near the surface of CVD graphene on Ge(110) locally aggregated hydrogen confined in the interface to form H_2-filled bubbles with controllable size and shape (Figure 1C,b) [37]. Additionally, laser irradiation is capable of actuating confined chemicals. Lee and colleagues exfoliated graphene from highly ordered pyrolytic graphite (HOPG), which had been chemically treated to intercalate ClF_3 between the graphite layers, onto an SiO_2/Si substrate. When irradiated with a 532-nm laser, the interface-confined ClF_3 sublimated and elastically bulged the graphene to form a bubble (Figure 1C,c) [38]. Laser irradiation has also been used to create graphene bubbles filled with liquid nitrogen [39]. The 2D crystals suspended over microcavities (referred to as 'drumheads' because of their likeliness to the musical instrument) also respond to external stimuli to form bubbles. These

drums could be inflated by pressure (Figure 1D,a) [40,41] or actuated through an electrical field (Figure 1D,b) [42].

Characterization of Bubble Content

Indirect Evidence

Characterizing bubble content is essential to understand how the trapped matter influences the chemistry and physics of 2D material bubbles. Due to the micro- and nanoscale size and extremely small volume of these bubbles, it is difficult to directly characterize the trapped matter via chemical analysis techniques like mass spectrometry. Moreover, the chemical diversity of the trapped matter, which is influenced by the fabrication method and environmental conditions, adds difficulty in characterizing the content of these bubbles. Indirect observations, however, could circumvent these difficulties and provide insights into the composition of the trapped matter and the conditions under which these bubbles form.

One method of inferring the type of matter that gets trapped in 2D material bubbles is to understand the chemical composition of the matter that rests on the surface of the 2D material and target substrate prior to assembly (Figure 2A). This line of reasoning assumes the surface matter unchangeably becomes the content of the bubbles after the surface becomes the interface. Various studies have shown that water and hydrocarbons readily adsorb onto the surface of 2D materials in quantities large enough to affect the macroscopic wetting behavior of their surfaces [10,15,43], making these chemicals likely candidates for the trapped matter. Additionally, if polymers are involved in the transfer process, either as stamps or adhesives to exfoliate monolayers from a bulk crystal, the surface and interface of the 2D material can be contaminated with polymer residues [44].

The shape and areal density of the bubbles depend heavily on the environmental conditions, namely humidity and temperature, under which the sample is fabricated. Cao and colleagues claimed that graphene/HOPG bubbles trapped adsorbed water on the surface of HOPG, allowing for the visualization of nanometer-scale water droplets [45]. The number of graphene/HOPG bubbles in a given area depended on the relative humidity of the ambient environment in which graphene was layered onto HOPG. Fabricating these bubbles in a dry environment resulted in fewer bubbles, suggesting that the content of the bubbles was water (Figure 2B) [45]. Similarly, the number of bubbles formed in a given area has been used to infer the type of gas trapped in graphene/graphite bubbles formed through electrolysis [36]. The temperature of the environment affects the formation of bubbles as well. Pizzocchero and colleagues observed that bubbles were less likely to form when graphene was layered onto hBN at temperatures above 110°C (Figure 2C) [13]. The authors suggested that the contents of these bubbles are likely water because the temperature required for bubble-free transfer is close to the boiling point of water.

Physical manipulation of the bubbles, ranging from deflating, poking, scratching, and bursting, is another intuitive way to probe bubble content. Deflation rates of the bubbles, measured by the change in bubble height and radius, depend on the phase and types of chemicals trapped in the bubble, as larger trapped molecules may require more time to diffuse through the interface. N_2-filled drumhead bubbles were found to deflate completely over the course of 7 days [46], while bubbles pressurized with liquid remained inflated for 6 months or more [47,48]. When substrate-supported bubbles were scratched with a sharp AFM tip, some of the liquid content escaped through the tear, while some remained as the torn edges of the 2D crystal re-adhered to the substrate, validating the fluidic nature of the confined material (Figure 2D) [16]. Bubbles can burst without external probing due to an overabundance of internal pressure as well. Pressure inside the bubble can build up through voltage-induced hydrolysis, causing the 2D

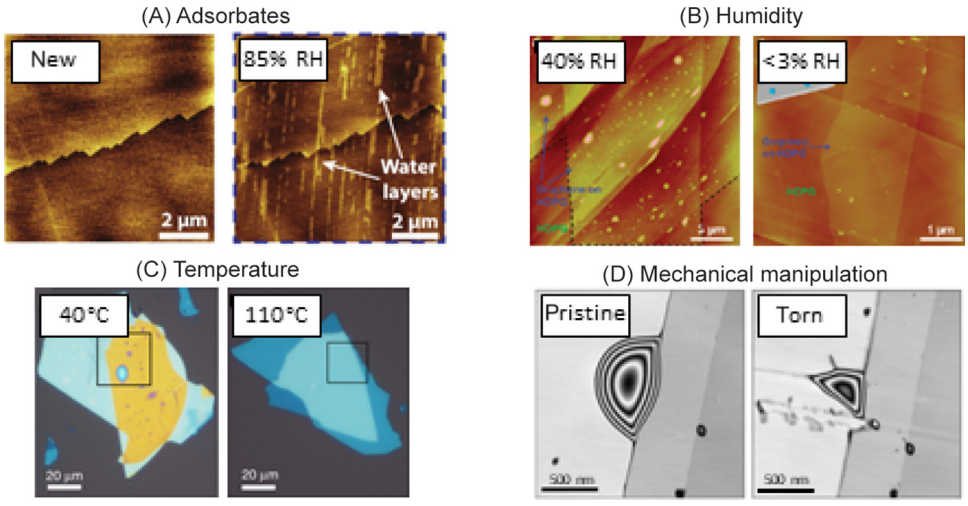

Figure 2. Indirect Methods of Determining Trapped Matter. (A) Atomic force microscopy (AFM) topographic images comparing the same region of MoS_2 immediately after the flake was exfoliated (left) and after the flake had been exposed to a high relative humidity (RH) environment. (B) AFM topographic images comparing a graphene/graphite sample fabricated in ambient conditions (left) with a different graphene/graphite sample prepared at low RH (right). (C) Optical micrograph of a graphene/hBN stack stamped onto another hBN flake. Bubbles appeared after stamping was carried out at 40°C (left). By contrast, bubbles did not form when graphene/hBN was stamped at 110°C (right). (D) AFM topographic images of a pristine graphene/hBN bubble at the boundary of single-layer (lighter grey) and bilayer (darker grey) graphene. The bubble was torn with an AFM tip, causing some of the trapped matter to escape before the graphene crystal re-adhered to the hBN (right). In order of their appearance, figures are adapted from [10,13,16,45], with permission.

material to rupture [47]. Likewise, graphene/hBN bubbles have been shown to burst when annealed in a vacuum chamber at 500°C [8]. Uwanno and colleagues attributed this rupturing to the reaction between graphene and the oxygen trapped in the bubbles, as well as the sp^2 bonds breaking due to the high strain in the bulged graphene [8].

Spectroscopic Analysis of 2D Material Bubbles

In contrast to indirect evidence, the spectroscopic methods displayed in Figure 3 allow for a more detailed characterization of the trapped content. Electrons and various wavelengths of light are able to transmit through the confining 2D material and probe the chemical composition of the sample without exposing the trapped matter to further contamination. Near-ambient pressure X-ray photoelectron spectroscopy (NAP-XPS) has been used to study the chemistry involved in the formation of N_2-filled bubbles (Figure 3A) [49]. XPS performed under vacuum has been also been used to measure the surface coverage of hydrocarbons [43]. In fact, hydrocarbon contamination in air-exposed samples is often used to calibrate XPS spectra, a procedure that has recently received significant scrutiny [50]. The contents of 2D material bubbles have been directly studied using spectroscopy by exposing the cross-section of a bubble with focused ion beam milling and analyzing the cross-section with electron spectroscopy (Figure 3B) [16]. Energy dispersive X-ray (EDX) spectroscopy and electron energy loss spectroscopy analyses of the trapped matter suggested that these bubbles are filled with hydrocarbons [16]. EDX has also been used to map the chemical distribution of Co_3O_4 nanoparticles trapped in graphene liquid cells (GLCs) filled with an $LiPF_6$ electrolyte solution (Figure 3C) [51]. Transmission electron microscopy (TEM) imaging of GLCs allows for direct observation of the bubble contents, which enables studies on how the environment affects the trapped materials. For example, TEM was used to observe square ice in water confined between two graphene layers at room temperature [52] (Figure 3D). The results of this study had been questioned due to the possibility of salt

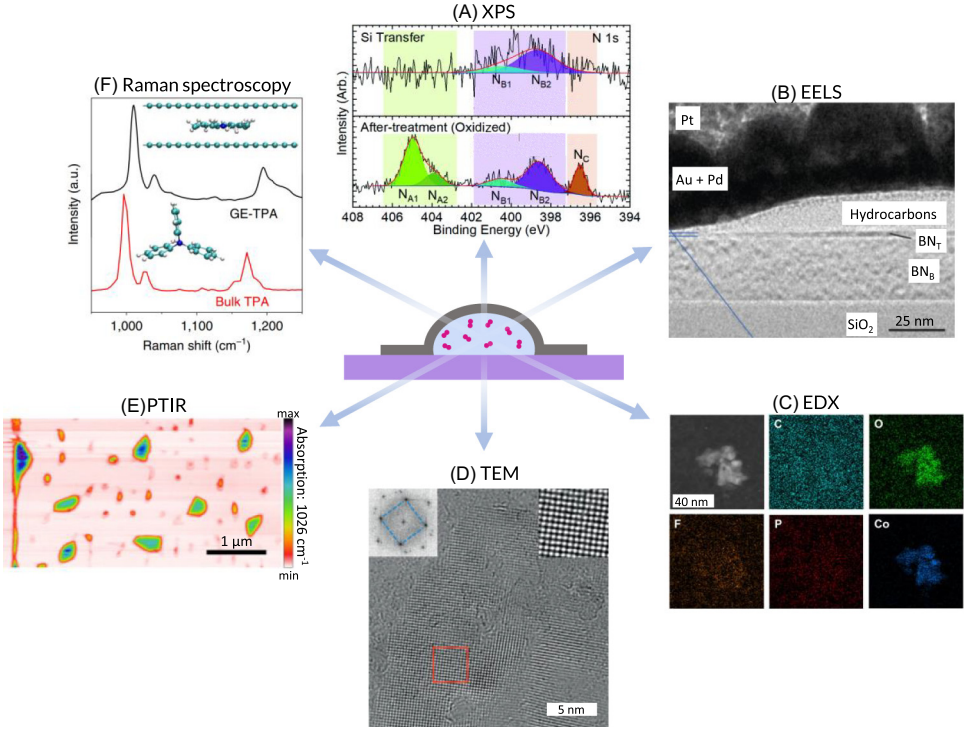

Figure 3. Using Spectroscopy to Identify Trapped Matter. (A) X-ray photoelectron spectra of the N 1 s peak in a graphene/Cu sample with bubbles. The N_{A1}, N_{A2}, and N_C peaks disappeared after the graphene was transferred onto Si, indicating that the trapped gas had escaped the bubbles. (B) Electron energy-loss spectroscopy (EELS) analysis of the graphene/hBN interface material reveals that the trapped contaminants are mostly hydrocarbons that became hardened during ion milling. (C) High-angle annular dark-field scanning transmission electron microscopy (HAADF-STEM) images of Co_3O_4 nanoparticles in an $LiPF_6$ liquid electrolyte solution and corresponding energy dispersive X-ray spectroscopy (EDX) elemental mappings show the element distribution in the graphene liquid cell (GLC). (D) Transmission electron microscopy (TEM) image of square ice inside a GLC. Inset figures display a Fourier transform of the TEM image (top left) and the magnified region outlined in red (top right). (E) Photothermal induced resonance (PTIR) absorption mapping of a WSe_2/hBN sample with bubbles. The absorption at 1026 cm^{-1} corresponds to Si-O-Si bond stretching of polydimethylsiloxane (PDMS) molecules trapped inside the bubbles. (F) Raman spectra of triphenyl amine (TPA) in a graphene/graphene bubble (bulk TPA) and confined in a flat graphene-encapsulated interface (GE-TPA). Inset images show the standard molecular structure of TPA (bottom) and the modified structure of TPA when confined at the graphene/graphene interface calculated using molecular dynamics (top). In order of their appearance, figures are adapted from [16,19,49,51,52,54], with permission.

contaminants in the aqueous environment [53]. Other types of spectroscopic methods, such as Raman and AFM-based photothermal infrared (PTIR) spectroscopy, can also identify a wide range of materials trapped inside the bubbles at relatively low photon energies, which decreases the probability of damaging the sample. For example, PTIR was used to identify the polymer residues in TMD/hBN bubbles (Figure 3E) [54], while Raman spectroscopy has been used to identify chemicals deliberately introduced in graphene/graphene bubbles (Figure 3F) [19].

Chemical Activities inside the Bubbles

2D material bubbles are a unique system that confines trapped matter into small volumes, while the vdW attraction between the adjoining surfaces and the elastic tension of the 2D material pressurize the trapped matter. In liquid-filled bubbles, the **Laplace pressure** resulting from the energy difference across the curved liquid–solid interface, also contributes to the bubble pressure

[55]. The contribution of each phenomena towards the total bubble pressure is unclear, especially at small length scales where the influence of **elastocapillarity** may dominate the mechanical behavior of the bubble system [56]. This has motivated several studies to determine the magnitude of pressure inside the bubbles and to utilize these pressurized environments to enable high-pressure chemistry. The pressure level inside 2D material bubbles is debated in the literature as the pressure is typically inferred by indirect means. The pressure inside the GLC is expected to be as low as ambient pressure due to the observation of H_2 bubbles nucleating from the aqueous environment under electron irradiation [29]. In addition to gas precipitates, the conditions under which solutes crystallize from the aqueous environment have been used to estimate pressure. For example, $CaSO_4$ was reported to crystalize in the GLC under TEM observation at temperatures ranging from 100°C to 150°C, which corresponds to a pressure of ~100 kPa to ~230 MPa (on the same order of the atmospheric pressure) based on the phase diagram [57]. Bubbles on rigid substrates are a distinct environment from GLCs because the rigid substrate provides additional constriction on the bubble, which could enable much higher pressure inside the bubbles. Theoretical models of 2D material bubbles have been used to estimate the pressure inside both liquid- and gas-filled bubbles. These models suggest that the bubble pressure scales inversely with the radius of the bubble and also depends on the stiffness of the confining 2D material as well as the shear strength of the interface [48,58]. Many studies on gas-filled bubbles use analytically derived equations that consider the compressibility of the trapped matter, resulting in estimates that are typically in the MPa range for bubbles with radii that are typically 100s of nm [36,38,59]. GPa pressures have been reported by applying the ideal-gas model to bubbles consisting of a few Ne atoms [27]. Theoretical modeling of liquid-filled bubbles, which accounts for the incompressibility of the trapped liquid but neglects the contribution of Laplace pressure, also predicts MPa-range bubble pressure for bubbles of similar sizes (e.g., 7 MPa for a MoS_2/Al_2O_3 bubble with a radius of 50 nm) [48]. In addition to mechanistic modeling, phase transformation and chemical reactions could also provide indications for the bubble pressure. For example, graphene/Ir bubbles filled with Ar were found to have consistently polygonal shapes [60]. The authors suggested that the irregular shapes were due to Ar forming solid aggregates in the high-pressure bubble environment, which would require pressures above 5 GPa based on the phase diagram of Ar [60]. GPa magnitudes of pressure have also been reported for graphene/diamond bubbles when annealed at high temperature and have been utilized as nanoscale hydrothermal anvils [61,62]. These water-filled graphene bubbles have been shown to covalently bond with its diamond (100) substrate when annealed at 1275 K for 45 minutes in ultra-high vacuum (Figure 4A) [61]. The covalent bonds at the interface formed from the dehydrogenation of hydrogen-terminated diamond at elevated temperature created strongly sealed graphene bubbles [61]. Graphene/diamond bubbles have also been used to observe the irreversible oligomerization of buckminsterfullerene when heated to 873 K, which coincides with an estimated pressure of 2.2 GPa (Figure 4B) [62]. Theoretical and computational studies suggested that the extreme pressures available inside graphene bubbles could enable unique thermodynamic states for the trapped matter, including forbidden geometries at low temperature for ethane-filled bubbles [63] and solid, liquid, or gaseous Ar (Figure 4C) [64,65].

Arguably, the most popular chemical application of 2D material bubbles is the use of GLCs for TEM imaging, which allows for the *in situ* observation of the nanoscale kinetics of the trapped matter. This subject has been extensively reviewed in other articles detailing their capabilities [66], preparation methods [67], and advantages over conventional encapsulation methods [68]. Imaging chemical and biological samples in the ultra-high vacuum environment required for TEM requires the use of a liquid cell to encapsulate the sample. The thinness, electrical conductivity, mechanical robustness, and small lateral dimensions of GLCs enable the study of a variety of dynamic processes, including the formation (Figure 4D) [69] and dissolution (Figure 4E) [70] of

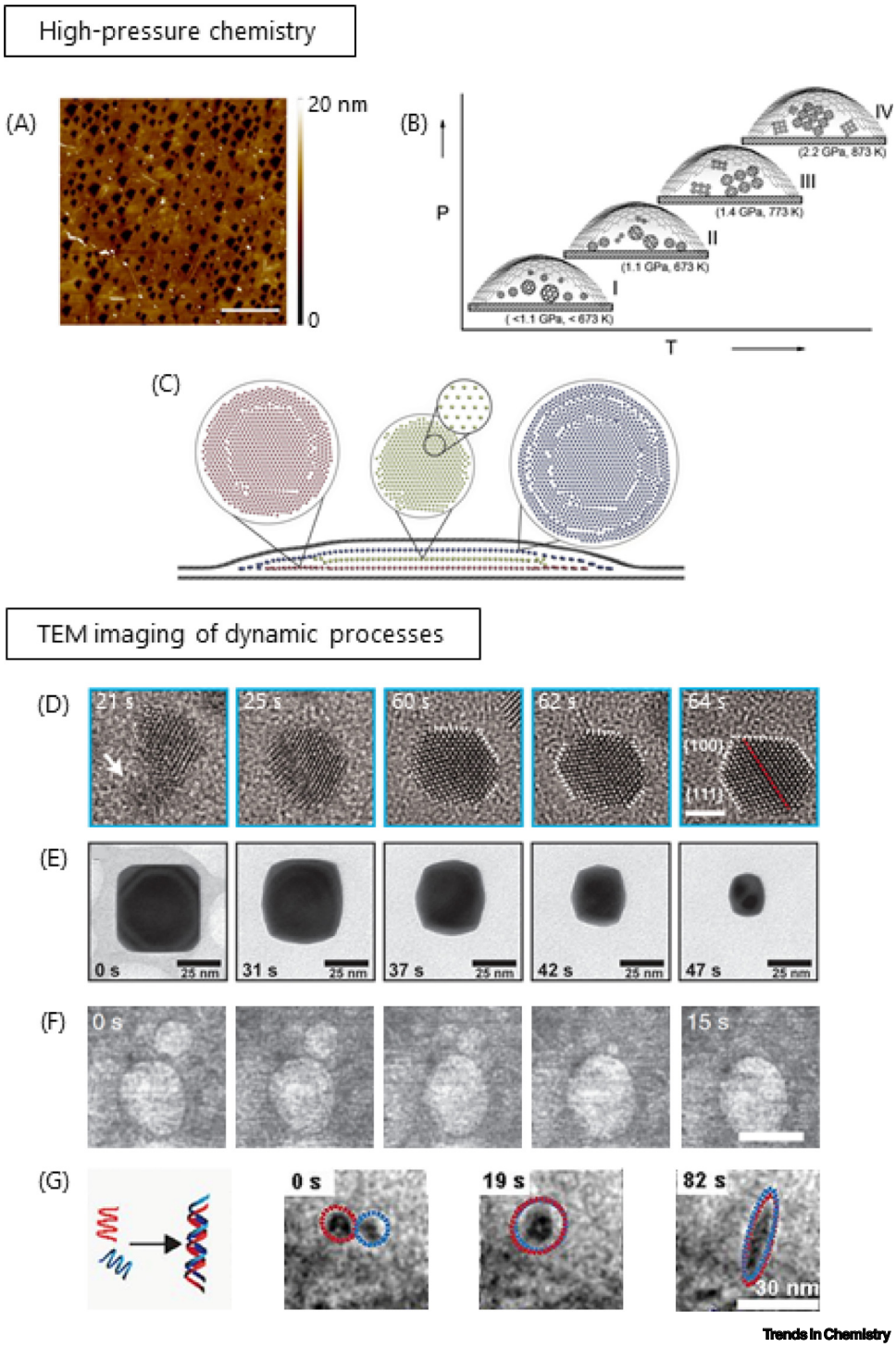

Figure 4. Chemical Activities inside Bubbles. (A) Atomic force microscopy (AFM) micrograph of voids that form in diamond after water-filled graphene bubbles react with the substrate at high temperature. (B) Schematic drawing of the oligomerization of C_{60} under high temperature and pressure in graphene bubbles. (C) A simulated graphene bubble filled with Ar. Inside this bubble, Ar is in the solid state and exhibits face-centered cubic and hexagonal close-packed crystal

(Figure legend continued at the bottom of the next page.)

nanocrystals, **Ostwald ripening** of gas bubbles (Figure 4F) [71], and even the hybridization of DNA molecules (Figure 4G) [72]. Notably, liquid cells fabricated from other types of 2D materials [73], including heterostructures, offer new environments to observe confined chemistry, such as the epitaxial growth of Pt nanocrystals on MoS_2 substrates [74].

In addition to their use in electron microscopy, gas-filled bubbles were also used to isolate graphene from either its metallic substrate or bulk crystal. After CVD graphene was grown on a metallic substrate, it was lifted off from its growth substrate using H_2 bubbles generated at the interface by electrochemical catalysis [75]. Likewise, graphene can be exfoliated from bulk graphite using a similar electrochemical process [76].

Additionally, solid inclusions have been used to shape 2D material bubbles for device applications, including supercapacitors [77], Li-ion battery anodes [78], and memristive Janus particles [79].

Bubble Physics

Mechanical strain applied to 2D materials modulates a wide range of their material properties (a phenomenon known as strain engineering) and enables the study of unprecedented physics in 2D materials. The methods to strain 2D materials are numerous and have been well-summarized in other reviews [80,81]. Bubbles have also been applied for 2D material strain engineering because of their versatile fabrication and characterization methods, as detailed earlier. Furthermore, straining atomically thin 2D materials through the inflation or deflation of bubbles is a relatively simple and easy-to-observe process compared with conventional techniques such as point loading by AFM or micro-mechanical loading frames [82,83]. Bulged 2D materials can achieve a considerable strain level, which can be controlled by the degree of inflation [80,84]. Although not yet widely explored, inflating suspended 2D materials over microwells of different geometries could induce a variety of strain fields in addition to uniaxial or equibiaxially straining. The viability of using strain engineering to tune the properties of 2D materials hinges on the deterministic application of strain to 2D materials. This has led to extensive experimental and theoretical efforts to understand the geometry-strain relations in bubbles, factors that influence the bubble geometry, and the strain magnitude and distribution.

The strain distribution of 2D materials confining circular bubbles has been related to the bubble height and radius through analytical models [48,58,85]. These distributions have been supported by Raman mapping [85–87]. Controlling the height and radius of these bubbles is key to controlling strain. The radius of 2D material drumheads is often prescribed by the size of holes prepatterned on the substrate, while the height can be controlled by the applied pressure (Figure 5A) [40,86,88]. However, when the pressure is substantial enough to cause the 2D material to delaminate from the substrate, both the radius and the height of the bubble increase with the pressure, while the aspect ratio (height:radius ratio) of the bubble remains a constant [40,89]. This limitation of the aspect ratio implies that there is an upper limit for the strain developable via pressurized bubbles as its magnitude scales as the square of the aspect ratio [85]. For spontaneously formed bubbles, their size is controlled by the volume and compressibility of the trapped substance [48,58], but their aspect ratio has been found to be

structures. (D–G) Dynamic chemical processes visualized using graphene liquid cells. (D) A smaller Pt nanocrystal (indicated by the white arrow) coalesces with another Pt nanocrystal and forms a twin boundary (red broken line). (E) $FeCl_3$ and electron beam irradiation cause a gold cube to etch into a tetrahexahedron. (F) Ostwald ripening of two gas bubbles of different sizes in water. (G) Two single-stranded DNA molecules hybridize to form a double-stranded helix. In order of their appearance, figures are adapted from [61,62,64,69–72], with permission.

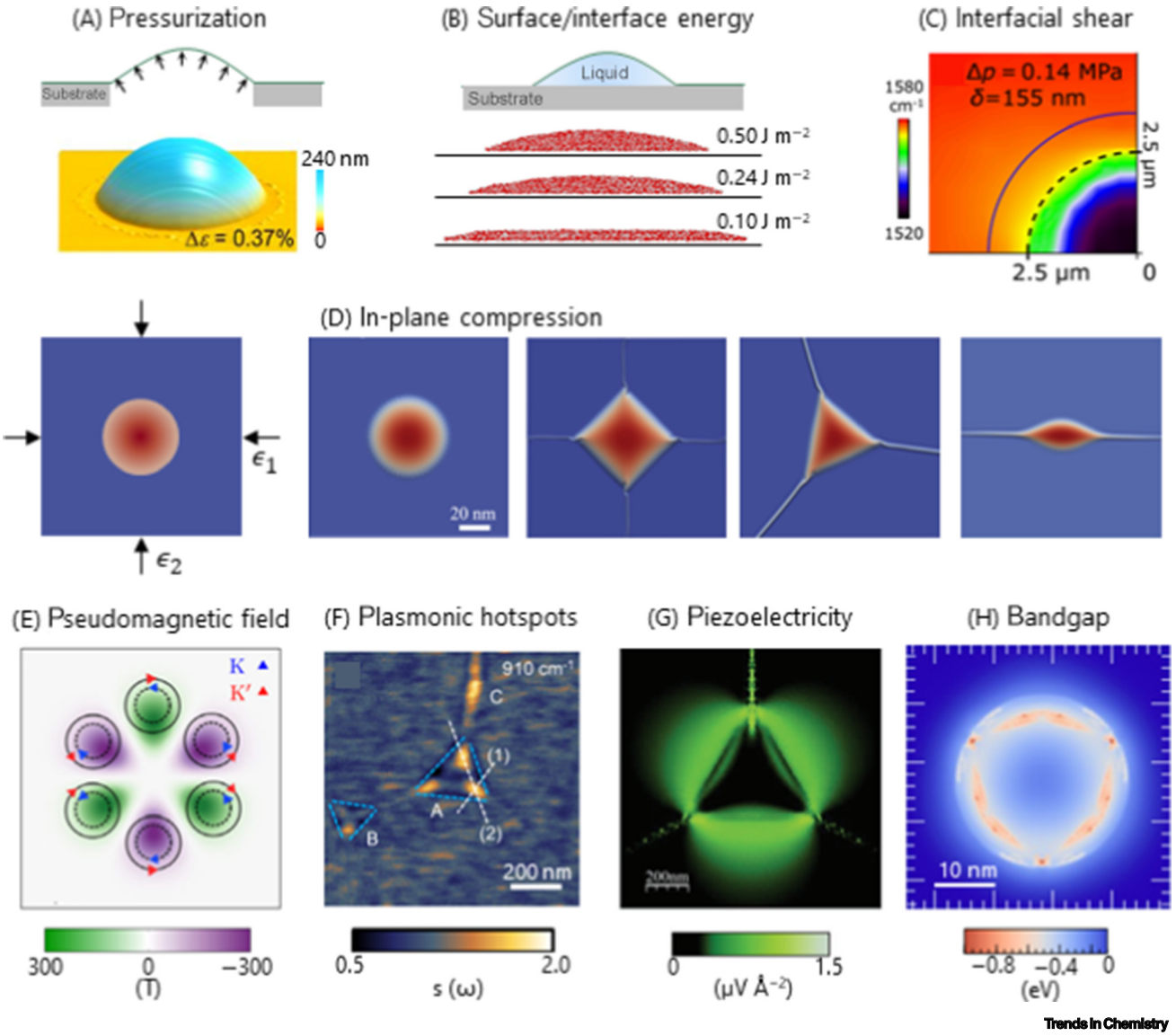

Figure 5. The Physics of 2D Material Bubbles. (A) Cross-sectional drawing of a gas-filled 2D material drumhead (top) and atomic force microscopy (AFM) topographic image of a graphene/SiO_2 drumhead pressurized to a strain level of 0.37% (bottom). (B) Cross-sectional drawing of a liquid-filled graphene bubble (top). Simulations show that the aspect ratio of the bubble increased with increasing adhesion energy between the 2D material (not shown) and substrate. (C) Raman mapping of a pressurized graphene/SiO_2 drumhead demonstrated how graphene slides when pressurized. The broken arc indicates the radius of the SiO_2 microwell and the unbroken arc defines the limit of the shear zone. (D) Simulations demonstrating the different shapes and wrinkles that can form by a circular graphene bubble when various types of in-plane residual compression ($_1$, $_2$) were in the graphene. (E) Gaussian deformation of graphene induces a threefold symmetric pseudomagnetic field (PMF) with different fields experienced in the *K* and *K′* valleys as indicated by the red and blue vortices. (F) Nano-IR image of hBN bubbles, marked A, B, and C, taken at $\omega = 910$ cm^{-1} with bubble boundaries marked with blue broken lines. The shift in near-field scattering amplitude, *s*, shows the location of plasmonic hotspots in the bubbles. (G) An energy density plot of a simulated hBN bubble shows strain-induced changes in the electric field around the bubble. (H) Wrinkling around the edge of a simulated MoS_2 bubble creates pockets of strain, which leads to band gap shifts in those regions measured in eV. In order of their appearance, figures are adapted from [48,86,92,94,96,104,110,111], with permission.

size independent [37,90]. In particular, for liquid-filled bubbles, the aspect ratio is related to the ratio of interfacial energies to the in-plane stiffness of the 2D material [48]. This understanding opens opportunities to tune the bubble geometry via interfacial energies, including the surface tension of the confining liquid and the 2D material–substrate adhesion (Figure 5B) [42,91].

A thorough understanding of the factors that influence strain and strain distributions in bubbles paves the way for understanding strain-coupled physics and the deterministic strain engineering in 2D materials (Box 1). This unique coupling between strain and electronic properties has resulted in several studies on the tuning of **pseudomagnetic fields (PMFs)**, band gaps, piezoelectricity [92,93], and surface plasmons [94]. PMFs result from the nonuniform strain distribution within graphene bubbles, with gigantic magnitudes ranging from 240 to 600 Tesla (T) (Figure 5E) [35,95,96]. The intensity of the PMF scales with the magnitude of strain gradient, while the spatial distribution of the PMF varies with the geometry of the bubble [97]. PMFs in bubbles could be exploited in valley filtering and valley splitting devices [96]. Graphene bubbles have also been shown to confine plasmonic hotspots, with distributions controlled by the bubble size and shape (Figure 5F) [94]. More recently, bubbles of monolayer hBN, an insulating 2D material, exhibited strain-induced changes in the local electric field, which is an indicator of piezoelectricity (Figure 5G) [92].

Strain can also tune band gaps in semiconducting TMDs. Such effect has been measured for monolayer and multilayer MoS_2. Lloyd and colleagues demonstrated that biaxial strain applied to monolayer MoS_2 drumheads decreases the optical band gap at a rate of –99 meV per percent

Box 1. Interface Sliding around 2D Material Bubbles

When translating the geometry of a bubble into strain fields, the slippage of the 2D material–substrate interfaces plays a significant role in the magnitude of strain accessible within the bubble region. Dai and colleagues studied the development of strain in 2D material bubbles by comparing two graphene drumheads: a strong shear-strength interface (graphene/SiO_2), and a weak shear-strength interface (graphene/graphite) (see Figure 5C in the main text). Both the analytical model and Raman mapping showed that the weak interface allows for the in-plane deformation of the 2D material in the substrate-supported region around the bubble, while bubbles with a strong interface inhibit this in-plane deformation. The restriction of in-plane deformation allows for a much greater magnitude of strain to develop in bubbles with stronger interfaces [85]. Whether the interfacial slippage is trivial enough to warrant a strong shear interface depends on the competition of the deformation level or aspect ratio (that drives the slippage) and the detailed interfacial shear strength (that resists the slippage). In general, most spontaneously formed bubbles could be considered to have weak interfaces [48]. Pressurized bubbles are closer to having strong interfaces as long as the substrate is not crystalline [48]. The interfacial slippage also plays a significant role in mechanical metrologies based on 2D material bubbles, including the extraction of the work of separation/adhesion of various 2D material–substrate interfaces [40,48], the bending and stretching stiffness of 2D materials [40,86,88], and the shear strength of 2D material interfaces [86,87].

Due to interfacial slippage, bubbles could appear elliptical when they are close to the edge of the 2D material, which breaks the axial symmetry of the problem (Figure I) [48]. In this case, though previous models for circular bubbles become invalid, it is expected that the lack of confinement at the edge would cause a further reduction of the strain achievable in the bubble. In experiments, bubbles take a variety of geometric shapes, ranging from circular to polygonal, even when they are far away from the edge of the 2D flake [111]. This transition is understood to originate from residual compressive strain in the 2D materials (see Figure 5D in the main text) [12,111]. The interplay between elastic energies and interfacial adhesion can result in the formation of straight edges and wrinkles [111–113]. In fact, at larger scales, the shapes of droplets encapsulated by elastic films can be tuned by tensile strain to achieve elliptical or square shapes [114], suggesting the control of liquid bubble shapes through pretension.

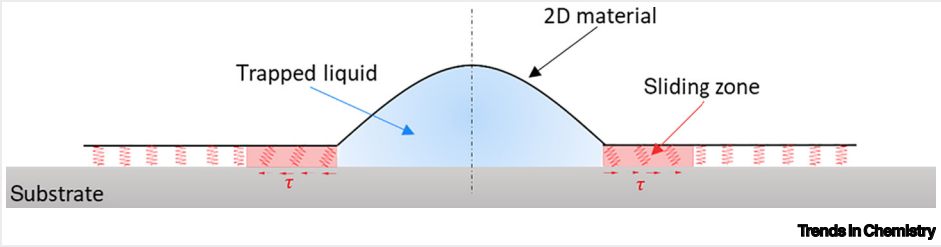

Figure I. Axial Symmetric Schematic of a Liquid-Filled 2D Material Bubble. The bulging deformation of the 2D material gives rise to the annular sliding zone around the bubble for weak shear interfaces. Adapted from [48], with permission.

of applied strain [98]. The center of the bubble has maximum strain, corresponding to the largest band gap reduction in the TMD. This band gap gradient has been shown to cause exciton drift towards the center of the bubble within the diffusion length of the electron–hole pair [99]. This gradient has been exploited to confine photon-excited electrical carriers [100] and to tune the wavelength of photons emitted from exciton recombination within the TMD bubble [101]. Moreover, bubbles have been used to create high areal density quantum light emitters in monolayer WSe_2 [102]. Strain in proton-irradiated monolayer MoS_2, WS_2, and WSe_2 bubbles triggered a **direct-to-indirect band gap transition** [99]. By contrast, multilayer MoS_2 bubbles simultaneously generated direct- and indirect-gap photoluminescence (PL) [103]. Wrinkling around the periphery of the TMD bubble, resulting from the bending rigidity of the 2D material, caused further strain localization in the shape of an annulus at the bubble edge (Figure 5H) [104]. This annular distribution of strain-localized exciton states has been investigated at room temperature in monolayer WSe_2 bubbles, where low-energy states formed the same 'doughnut-like' pattern as predicted in theoretical studies [105]. Additional unusual optical properties include optical bistability in graphene bubbles [106] and oscillations in the PL and Raman spectra of large graphene and TMD bubbles across the bubble profile [107,108].

Strain modulates the mechanical and frictional properties of the 2D materials in addition to their electronic properties. Crumpling in suspended graphene, which originates from static wrinkling and out-of-plane flexural phonons, is suppressed when the material is bulged. A transition from linear to nonlinear stress-strain behavior was observed between pretensioned and crumpled graphene drumheads [109]. Moreover, graphene bubbles pressurized to a strain of 0.6% exhibited extremely low friction coefficients when probed with an AFM cantilever tip because the tensioned graphene conformed less to the tip than relaxed graphene [110].

Concluding Remarks

2D material bubbles have been largely viewed as inevitable defects of the transfer process. While these bubbles remain unwanted in many devices, the detailed examination of why and how bubbles form at 2D material interfaces has enabled new avenues of research and applications. They may be formed through numerous methods, as discussed in this review. The confining 2D material can be selected with desired electrical, mechanical, or chemical properties, along with the phase and chemical composition of the trapped matter. The large magnitude of pressure inside the bubble can enable high-pressure chemistry at the nanoscale, while simultaneously serving as a window to observe the dynamic chemical processes through various spectroscopic methods. In turn, the deformation of the confining 2D material allows for strain-enabled physics, such as PMFs and bang gap engineering, and for the measurement of nanoscale mechanical properties, like interfacial shear. However, the many variables that ultimately determine the physics and chemistry of 2D material bubbles also drastically complicate the bubble system itself, making a concrete determination of their intrinsic and extrinsic properties difficult (see Outstanding Questions). Advancing the applications of these bubbles requires an understanding of the complete details of the 2D material bubble system, which necessitates coordinated effort across multiple research disciplines.

Acknowledgments

D.A.S. acknowledges support from the National Science Foundation (NSF) Graduate Research Fellowship Program, the Virginia and Ernest Cockrell, Jr. Fellowship of UT Austin, and the Ford Foundation Dissertation Fellowship. Z.D. acknowledges the Graduate Continuing Fellowship from UT Austin. N.L. acknowledges the UT Austin CNS catalyst grant. D.A.S. thanks Mr Jiaming He of UT Austin for the helpful discussions on solid-state physics.

References

1. Novoselov, K.S. *et al.* (2004) Electric field effect in atomically thin carbon films. *Science* 306, 666–669
2. Shen, P.-C. *et al.* (2018) CVD technology for 2-D materials. *IEEE Trans. Electron Devices* 65, 4040–4052

Outstanding Questions

How does trapped matter travel through the 2D material–substrate interface to form bubbles and to deflate them? How does this process vary by chemical species or with 2D material–substrate type?

Although the use of indirect evidence and spectroscopic analysis has offered many insights into the composition of the bubbles, there remains an incomplete picture of all the chemicals trapped inside these bubbles. How can the limitations of these methods of inquiry be overcome to provide a detailed picture of all the chemicals present in the trapped matter?

To what degree are adventitious contaminants, such as water and hydrocarbons, present in bubbles fabricated under ambient conditions? How would the presence of these unaccounted contaminants affect the interpretations of previously reported chemical reactions in bubbles?

How does sample processing, such as thermal annealing and storage in ultra-high vacuum, affect the chemical contents of the bubbles?

How can the Laplace pressure of liquid-filled 2D material bubbles be modeled and simulated? Does this Laplace pressure have an appreciable effect on the pressure inside the bubble? A detailed understanding of how Laplace pressure, elasticity, and vdW attraction each contribute to the total bubble pressure could enable precise control of this pressure.

How can diverse or asymmetric strain fields be achieved by controlling the shape of 2D material bubbles? Precisely designed strain fields could be used to give rise to specifically desired strain-coupled fields, such as pseudomagnetic fields, and enable a higher level of control of those fields for their integration in devices.

Is it possible to build transient devices by leveraging the time-dependent nature of the bubbles?

Is it possible to use these highly deformable 2D material bubbles for the transport of liquids and particles at the 2D material interfaces?

3. Zhao, H. *et al.* (2019) Two-dimensional amorphous nanomaterials: synthesis and applications. *2D Mater.* 6, 032002
4. Liu, W. *et al.* (2017) A two-dimensional conjugated aromatic polymer via C-C coupling reaction. *Nat. Chem.* 9, 563–570
5. Zhang, W. *et al.* (2016) Van der Waals stacked 2D layered materials for optoelectronics. *2D Mater.* 3, 022001
6. Xiao, Y. *et al.* (2020) Moiré is more: access to new properties of two-dimensional layered materials. *Matter* 3, 1142–1161
7. Rosenberger, M.R. *et al.* (2018) Nano-"squeegee" for the creation of clean 2D material interfaces. *ACS Appl. Mater. Interfaces* 10, 10379–10387
8. Uwanno, T. *et al.* (2015) Fully dry PMMA transfer of graphene on h-BN using a heating/cooling system. *2D Mater.* 2, 041002
9. Wu, F. *et al.* (2020) Formation of coherent 1H–1T heterostructures in single-layer MoS_2 on Au(111). *ACS Nano.* 14, 16939–16950
10. Bampoulis, P. *et al.* (2016) Hydrophobic ice confined between graphene and MoS_2. *J. Phys. Chem. C* 120, 27079–27084
11. Kretinin, A.V. *et al.* (2014) Electronic properties of graphene encapsulated with different two-dimensional atomic crystals. *Nano Lett.* 14, 3270–3276
12. Jain, A. *et al.* (2018) Minimizing residues and strain in 2D materials transferred from PDMS. *Nanotechnology* 29, 265203
13. Pizzocchero, F. *et al.* (2016) The hot pick-up technique for batch assembly of van der Waals heterostructures. *Nat. Commun.* 7, 11894
14. Purdie, D.G. *et al.* (2018) Cleaning interfaces in layered materials heterostructures. *Nat. Commun.* 9, 5387
15. Li, Z. *et al.* (2016) Water protects graphitic surface from airborne hydrocarbon contamination. *ACS Nano* 10, 349–359
16. Haigh, S.J. *et al.* (2012) Cross-sectional imaging of individual layers and buried interfaces of graphene-based heterostructures and superlattices. *Nat. Mater.* 11, 764–767
17. Gasparutti, I. *et al.* (2020) How clean is clean? Recipes for van der Waals heterostructure cleanliness assessment. *ACS Appl. Mater. Interfaces* 12, 7701–7709
18. Xu, K. *et al.* (2010) Graphene visualizes the first water adlayers on mica at ambient conditions. *Science* 329, 1188–1191
19. Vasu, K.S. *et al.* (2016) Van der Waals pressure and its effect on trapped interlayer molecules. *Nat. Commun.* 7, 12168
20. Zong, Z. *et al.* (2010) Direct measurement of graphene adhesion on silicon surface by intercalation of nanoparticles. *J. Appl. Physics.* 107, 026104
21. Wu, S. *et al.* (2020) Super-slippery degraded black phosphorus/silicon dioxide interface. *ACS Appl. Mater. Interfaces* 12, 7717–7726
22. Wood, J.D. *et al.* (2014) Effective passivation of exfoliated black phosphorus transistors against ambient degradation. *Nano Lett.* 14, 6964–6970
23. Mirabelli, G. *et al.* (2016) Air sensitivity of MoS_2, $MoSe_2$, $MoTe_2$, HfS_2, and $HfSe_2$. *J. Appl. Phys.* 120, 125102
24. Budania, P. *et al.* (2017) Long-term stability of mechanically exfoliated MoS_2 flakes. *MRS Commun.* 7, 813–818
25. Tedeschi, D. *et al.* (2019) Controlled micro/nanodome formation in proton-irradiated bulk transition-metal dichalcogenides. *Adv. Mater.* 31, e1903795
26. He, L. *et al.* (2019) Isolating hydrogen in hexagonal boron nitride bubbles by a plasma treatment. *Nat. Commun.* 10, 2815
27. Wang, J. *et al.* (2016) Atomic intercalation to measure adhesion of graphene on graphite. *Nat. Commun.* 7, 13263
28. Herbig, C. *et al.* (2015) Xe irradiation of graphene on Ir(111): from trapping to blistering. *Phys. Rev. B* 92, 085429
29. Wang, C. *et al.* (2016) Precise in situ modulation of local liquid chemistry via electron irradiation in nanoreactors based on graphene liquid cells. *Adv. Mater.* 28, 7716–7722
30. Larciprete, R. *et al.* (2016) Self-assembly of graphene nanoblisters sealed to a bare metal surface. *Nano Lett.* 16, 1808–1817
31. Yasuda, S. *et al.* (2020) Confinement of hydrogen molecules at graphene–metal interface by electrochemical hydrogen evolution reaction. *J. Phys. Chem. C* 124, 5300–5307
32. Stolyarova, E. *et al.* (2009) Observation of graphene bubbles and effective mass transport under graphene films. *Nano Lett.* 9, 332–337
33. Kim, H.H. *et al.* (2013) Substrate-induced solvent intercalation for stable graphene doping. *ACS Nano* 7, 1155–1162
34. Jung, W. *et al.* (2014) Prevention of water permeation by strong adhesion between graphene and SiO_2 substrate. *Small* 10, 1704–1711
35. Lu, J. *et al.* (2012) Transforming Moiré blisters into geometric graphene nano-bubbles. *Nat. Commun.* 3, 823
36. An, H. *et al.* (2017) Graphene nanobubbles produced by water splitting. *Nano Lett.* 17, 2833–2838
37. Jia, P. *et al.* (2019) Programmable graphene nanobubbles with three-fold symmetric pseudo-magnetic fields. *Nat. Commun.* 10, 3127
38. Lee, J.H. *et al.* (2014) Nanometer thick elastic graphene engine. *Nano Lett.* 14, 2677–2680
39. Zhang, X. *et al.* (2020) Construction of position-controllable graphene bubbles in liquid nitrogen with assistance of low-power laser. *ACS Appl. Mater. Interfaces* 12, 56260–56268
40. Koenig, S.P. *et al.* (2011) Ultrastrong adhesion of graphene membranes. *Nat. Nanotechnol.* 6, 543–546
41. Yin, P. and Ma, M. (2018) Efficient and robust fabrication of micro-scale graphene drums. *ACS Appl. Nano Mater.* 1, 6596–6602
42. Georgiou, T. *et al.* (2011) Graphene bubbles with controllable curvature. *Appl. Phys. Lett.* 99, 093103
43. Li, Z. *et al.* (2013) Effect of airborne contaminants on the wettability of supported graphene and graphite. *Nat. Mater.* 12, 925–931
44. Rezania, B. *et al.* (2013) Influence of graphene exfoliation on the properties of water-containing adlayers visualized by graphenes and scanning force microscopy. *J. Colloid Interface Sci.* 407, 500–504
45. Cao, P. *et al.* (2011) The microscopic structure of adsorbed water on hydrophobic surfaces under ambient conditions. *Nano Lett.* 11, 5581–5586
46. Boddeti, N.G. *et al.* (2013) Graphene blisters with switchable shapes controlled by pressure and adhesion. *Nano Lett.* 13, 6216–6221
47. Tan, B.H. *et al.* (2020) Direct measurement of the contents, thickness, and internal pressure of molybdenum disulphide nanoblisters. *Nano Lett.* 20, 3478–3484
48. Sanchez, D.A. *et al.* (2018) Mechanics of spontaneously formed nanoblisters trapped by transferred 2D crystals. *Proc. Natl. Acad. Sci. U. S. A.* 115, 7884–7889
49. Zahra, K.M. *et al.* (2020) Intercalation, decomposition, entrapment – a new route to graphene nanobubbles. *Phys. Chem. Chem. Phys.* 22, 7606–7615
50. Greczynski, G. and Hultman, L. (2020) Compromising science by ignorant instrument calibration-need to revisit half a century of published XPS data. *Angew. Chem. Int. Ed. Engl.* 59, 5002–5006
51. Chang, J.H. *et al.* (2019) Graphene liquid cell electron microscopy of initial lithiation in Co3O4 Nanoparticles. *ACS Omega* 4, 6784–6788
52. Algara-Siller, G. *et al.* (2015) Square ice in graphene nanocapillaries. *Nature* 519, 443–445
53. Zhou, W. *et al.* (2015) The observation of square ice in graphene questioned. *Nature* 528, E1–E2
54. Schwartz, J.J. *et al.* (2019) Chemical identification of interlayer contaminants within van der Waals heterostructures. *ACS Appl. Mater. Interfaces* 11, 25578–25585
55. Ghodsi, S.M. *et al.* (2020) Assessment of pressure and density of confined water in graphene liquid cells. *Adv. Mater. Interfaces* 7, 1901727
56. Yoshida, H. *et al.* (2018) Dripplons as localized and superfast ripples of water confined between graphene sheets. *Nat. Commun.* 9, 1–9
57. Lehnert, T. *et al.* (2017) In situ crystallization of the insoluble anhydrite AII phase in graphene pockets. *ACS Nano* 11, 7967–7973
58. Yue, K. *et al.* (2012) Analytical methods for the mechanics of graphene bubbles. *J. Appl. Phys.* 112, 083512
59. Dollekamp, E. *et al.* (2016) Electrochemically induced nanobubbles between graphene and mica. *Langmuir* 32, 6582–6590
60. Zamborlini, G. *et al.* (2015) Nanobubbles at GPa pressure under graphene. *Nano Lett.* 15, 6162–6169
61. Lim, C.H.Y.X. *et al.* (2013) A hydrothermal anvil made of graphene nanobubbles on diamond. *Nat. Commun.* 4, 1–8
62. Lim, C.H. *et al.* (2014) Observing high-pressure chemistry in graphene bubbles. *Angew. Chem. Int. Ed. Engl.* 53, 215–219

63. Iakovlev, E. *et al.* (2019) Modeling of the phase transition inside graphene nanobubbles filled with ethane. *Phys. Chem. Chem. Phys.* 21, 18099–18104
64. Iakovlev, E. *et al.* (2017) Atomistic study of the solid state inside graphene nanobubbles. *Sci. Rep.* 7, 1–7
65. Zhilyaev, P. *et al.* (2019) Liquid-gas phase transition of Ar inside graphene nanobubbles on the graphite substrate. *Nanotechnology* 30, 215701
66. Ghodsi, S.M. *et al.* (2019) Advances in graphene-based liquid cell electron microscopy: working principles, opportunities, and challenges. *Small Methods* 3, 1900026
67. Textor, M. and de Jonge, N. (2018) Strategies for preparing graphene liquid cells for transmission electron microscopy. *Nano Lett.* 18, 3313–3321
68. Kashin, A.S. and Ananikov, V.P. (2019) Monitoring chemical reactions in liquid media using electron microscopy. *Nat. Rev. Chem.* 3, 624–637
69. Yuk, J.M. *et al.* (2012) High-resolution EM of colloidal nanocrystal growth using graphene liquid cells. *Science* 336, 61–64
70. Hauwiller, M.R. *et al.* (2018) Unraveling kinetically-driven mechanisms of gold nanocrystal shape transformations using graphene liquid cell electron microscopy. *Nano Lett.* 18, 5731–5737
71. Shin, D. *et al.* (2015) Growth dynamics and gas transport mechanism of nanobubbles in graphene liquid cells. *Nat. Commun.* 6, 1–6
72. Wang, H. *et al.* (2020) Intermediate states of molecular self-assembly from liquid-cell electron microscopy. *Proc. Natl. Acad. Sci. U. S. A.* 117, 1283–1292
73. Yang, J. *et al.* (2019) Liquid pockets encapsulated in MoS_2 liquid cells. *Microsc. Microanal.* 25, 1406–1407
74. Yang, J. *et al.* (2019) MoS_2 liquid cell electron microscopy through clean and fast polymer-free MoS_2 transfer. *Nano Lett.* 19, 1788–1795
75. Gao, L. *et al.* (2012) Repeated growth and bubbling transfer of graphene with millimetre-size single-crystal grains using platinum. *Nat. Commun.* 3, 1–7
76. He, P. *et al.* (2017) Kinetically enhanced bubble-exfoliation of graphite toward high-yield preparation of high-quality graphene. *Chem. Mater.* 29, 8578–8582
77. Chen, C.M. *et al.* (2012) Macroporous 'bubble' graphene film via template-directed ordered-assembly for high rate supercapacitors. *Chem. Commun.* 48, 7149–7151
78. Xu, Q. *et al.* (2018) SiOx encapsulated in graphene bubble film: an ultrastable Li-ion battery anode. *Adv. Mater.* 30, 1707430
79. Liu, P. *et al.* (2018) Autoperforation of 2D materials for generating two-terminal memristive Janus particles. *Nat. Mater.* 17, 1005–1012
80. Dai, Z. *et al.* (2019) Strain engineering of 2D materials: issues and opportunities at the interface. *Adv. Mater.* 31, 1805417
81. Deng, S. *et al.* (2018) Strain engineering in two-dimensional nanomaterials beyond graphene. *Nano Today* 22, 14–35
82. Benameur, M.M. *et al.* (2015) Electromechanical oscillations in bilayer graphene. *Nat. Commun.* 6, 1–7
83. Goldsche, M. *et al.* (2018) Tailoring mechanically tunable strain fields in graphene. *Nano Lett.* 18, 1707–1713
84. Darlington, T.P. *et al.* (2020) Facile and quantitative estimation of strain in nanobubbles with arbitrary symmetry in 2D semiconductors verified using hyperspectral nano-optical imaging. *J. Chem. Phys.* 153, 024702
85. Dai, Z. *et al.* (2018) Interface-governed deformation of nanobubbles and nanotents formed by two-dimensional materials. *Phys. Rev. Lett.* 121, 266101
86. Wang, G. *et al.* (2017) Measuring interlayer shear stress in bilayer graphene. *Phys. Rev. Lett.* 119, 036101
87. Kitt, A.L. *et al.* (2013) How graphene slides: measurement and theory of strain-dependent frictional forces between graphene and SiO2. *Nano Lett.* 13, 2605–2610
88. Wang, G. *et al.* (2019) Bending of multilayer van der Waals materials. *Phys. Rev. Lett.* 123, 116101
89. Lloyd, D. *et al.* (2017) Adhesion, stiffness, and instability in atomically thin MoS_2 bubbles. *Nano Lett.* 17, 5329–5334
90. Khestanova, E. *et al.* (2016) Universal shape and pressure inside bubbles appearing in van der Waals heterostructures. *Nat. Commun.* 7, 12587
91. Ghorbanfekr-Kalashami, H. *et al.* (2017) Dependence of the shape of graphene nanobubbles on trapped substance. *Nat. Commun.* 8, 15844
92. Ares, P. *et al.* (2020) Piezoelectricity in monolayer hexagonal boron nitride. *Adv. Mater.* 32, 1905504
93. Wang, W. *et al.* (2020) Visualizing piezoelectricity on 2D crystals nanobubbles. *Adv. Funct. Mater.* Published online November 11, 2020. https://doi.org/10.1002/adfm.202005053
94. Fei, Z. *et al.* (2016) Ultraconfined plasmonic hotspots inside graphene nanobubbles. *Nano Lett.* 16, 7842–7848
95. Levy, N. *et al.* (2010) Strain-induced pseudo–magnetic fields greater than 300 Tesla in graphene nanobubbles. *Science* 329, 544–547
96. Settnes, M. *et al.* (2016) Graphene nanobubbles as valley filters and beam splitters. *Phys. Rev. Lett.* 117, 276801
97. Qi, Z. *et al.* (2014) Pseudomagnetic fields in graphene nanobubbles of constrained geometry: a molecular dynamics study. *Phys. Rev. B* 90, 125419
98. Lloyd, D. *et al.* (2016) Band gap engineering with ultralarge biaxial strains in suspended monolayer MoS2. *Nano Lett.* 16, 5836–5841
99. Blundo, E. *et al.* (2020) Evidence of the direct-to-indirect band gap transition in strained two-dimensional WS 2, MoS 2, and WSe 2. *Phys. Rev. Res.* 2, 012024
100. Chirolli, L. *et al.* (2019) Strain-induced bound states in transition-metal dichalcogenide bubbles. *2D Mater.* 6, 025010
101. Tyurnina, A.V. *et al.* (2019) Strained bubbles in van der Waals heterostructures as local emitters of photoluminescence with adjustable wavelength. *ACS Photonics* 6, 516–524
102. Shepard, G.D. *et al.* (2017) Nanobubble induced formation of quantum emitters in monolayer semiconductors. *2D Mater.* 4, 021019
103. Luo, H.L. *et al.* (2020) Simultaneous generation of direct- and indirect-gap photoluminescence in multilayer MoS_2 bubbles. *Phys. Rev. Mater.* 4, 074006
104. Carmesin, C. *et al.* (2019) Quantum-dot-like states in molybdenum disulfide nanostructures due to the interplay of local surface wrinkling, strain, and dielectric confinement. *Nano Lett.* 19, 3182–3186
105. Darlington, T.P. *et al.* (2020) Imaging strain-localized excitons in nanoscale bubbles of monolayer WSe_2 at room temperature. *Nat. Nanotechnol.* 15, 854–860
106. Bao, Q. *et al.* (2015) Graphene nanobubbles: a new optical nonlinear material. *Adv. Opt. Mater.* 3, 744–749
107. Jia, Z. *et al.* (2019) Photoluminescence and Raman spectra oscillations induced by laser interference in annealing-created monolayer WS_2 bubbles. *Adv. Opt. Mater.* 7, 1801373
108. Huang, Y. *et al.* (2018) Raman spectral band oscillations in large graphene bubbles. *Phys. Rev. Lett.* 120, 186104
109. Nicholl, R.J.T. *et al.* (2017) Hidden area and mechanical nonlinearities in freestanding graphene. *Phys. Rev. Lett.* 118, 266101
110. Zhang, S. *et al.* (2019) Tuning friction to a superlubric state via in-plane straining. *Proc. Natl. Acad. Sci.* 116, 24452–24456
111. Zhang, K. and Arroyo, M. (2017) Coexistence of wrinkles and blisters in supported graphene. *Extreme Mech. Lett.* 14, 23–30
112. Zhang, K. and Arroyo, M. (2014) Understanding and strain-engineering wrinkle networks in supported graphene through simulations. *J. Mech. Phys. Solids* 72, 61–74
113. Dai, Z. *et al.* (2020) Radial buckle delamination around 2D material tents. *J. Mech. Phys. Solids* 137, 103843
114. Schulman, R.D. and Dalnoki-Veress, K. (2018) Droplets capped with an elastic film can be round, elliptical, or nearly square. *Phys. Rev. Lett.* 121, 248004